Geophysical Research Letters

RESEARCH LETTER
10.1029/2020GL090477

Key Points:

- Flow rate and pressure gradient during steady-state multiphase flow are measured experimentally
- The transition to a non-Darcy flow regime is quantified and predicted theoretically
- The theory makes accurate predictions for several rock types, fractional flows, and mobility ratios

Correspondence To:
Y. Zhang,
yihuai.zhang@imperial.ac.uk

Citation:
Zhang, Y., Bijeljic, B., Gao, Y., Lin, Q., & Blunt, M. J. (2021). Quantification of nonlinear multiphase flow in porous media. *Geophysical Research Letters*, *48*, e2020GL090477. https://doi.org/10.1029/2020GL090477

Received 25 AUG 2020
Accepted 23 JAN 2021

Quantification of Nonlinear Multiphase Flow in Porous Media

Yihuai Zhang[1], Branko Bijeljic[1], Ying Gao[1], Qingyang Lin[1], and Martin J. Blunt[1]

[1]Department of Earth Science and Engineering, Imperial College London, London, UK

Abstract We measure the pressure difference during two-phase flow across a sandstone sample for a range of injection rates and fractional flows of water, the wetting phase, during an imbibition experiment. We quantify the onset of a transition from a linear relationship between flow rate and pressure gradient to a nonlinear power-law dependence. We show that the transition from linear (Darcy) to nonlinear flow and the exponent in the power-law is a function of fractional flow. We use energy balance to accurately predict the onset of intermittency for a range of fractional flows, fluid viscosities, and different rock types.

Plain Language Summary Multiphase flow in porous media is described by an empirical extension of Darcy's law where flow rate is proportional to pressure gradient. Darcy's law is used to quantify and design a wide variety of processes including carbon dioxide storage in the subsurface, and air and moisture flows through materials as diverse as soils and surgical masks. However, as flow rate increases, this linear Darcy law breaks down with a transition to a nonlinear intermittent flow regime. Through an extensive set of experimental measurements, we quantify the relationship between flow rate and pressure gradient. A theory based on energy balance accurately predicts the transition to intermittency. Our work quantifies multiphase flow over a wide range of conditions.

1. Introduction

The flow of multiple fluids in porous materials occurs in a wide variety of important natural and engineered settings relevant for the understanding of geological CO_2 storage, geothermal energy extraction, magma flow, oil and gas recovery, contaminant transport, flow in fuel cells, microfluidics in drug delivery, and the effectiveness of respirators and surgical masks (see for instance, Blunt, 2017; Gjennestad et al., 2020; Iglauer et al., 2019; Pak et al., 2015; Reynolds & Krevor, 2015; Zhang et al., 2019; Zhao et al., 2018). It is assumed that the flow rate is proportional to the pressure gradient, governed by a Darcy-type law (Blunt, 2017; Muskat, 1937; Muskat & Meres, 1936),

$$q_p = -\frac{k_{rp}K}{\mu_p}(\nabla P_p - \rho_p g), \tag{1}$$

where q_p is the volume of phase p flowing per unit area per unit time, k_{rp} is the relative permeability, K is the absolute permeability, μ_p is the viscosity, ∇P_p is the pressure gradient, and $\rho_p g$ is the contribution of gravity.

In this work, we will consider two-phase horizontal flow of a nonwetting phase, nw, and a wetting phase, w, where the gravitational term is zero. Also we will study steady-state flow where the macroscopic capillary pressure (the average pressure difference between the phases) does not vary across the sample: hence $\nabla P_p = \nabla P$ for both phases. In this case, we can write the total Darcy flux $q_t = q_{nw} + q_w$ as

$$q_t = -\lambda_t K \nabla P, \tag{2}$$

where λ_t is the total mobility: $\lambda_t = k_{rw}/\mu_w + k_{rnw}/\mu_{nw}$.

The relative magnitude of viscous and capillary forces can be encapsulated in the capillary number, defined for each phase as $Ca_p = \mu_p q_p/\sigma$, where σ is the interfacial tension between the phases. We also define a total capillary number (Spurin et al., 2019b)

$$Ca = \frac{q_t}{\sigma\left(\frac{1-f_w}{\mu_{nw}} + \frac{f_w}{\mu_w}\right)}, \tag{3}$$

where $f_w = q_w/q_t$ is the fractional flow. For a displacement with fixed fractional flow, but where the flow rate varies, Equation 2 implies a linear relationship: $\nabla P \sim Ca$.

It is well known that this linear law breaks down when, at the pore scale, viscous forces become comparable to capillary forces with a threshold value of Ca of around 10^{-3} (Blunt, 2017; Lake, 1989): in this regime, the two-phases flow together through the pore space with a fractional flow which is proportional to saturation. Recently, however, a body of research has demonstrated that multiphase flow in porous media has a complex dynamics even at low Ca where displacement is still dominated by capillary forces at the pore scale (Armstrong & Berg, 2013; Berg et al., 2013; Datta et al., 2014a, 2014b; Reynolds et al., 2017; Rücker et al., 2015). It has been proposed that there is a transition from capillary-dominated to an intermittent flow regime with a power-law dependence between pressure gradient and flow rate

$$\nabla P \sim Ca^a \tag{4}$$

with $1 > a > 0$ for $Ca > Ca^i$. Tallakstad et al. (2009) conducted steady-state two-phase simultaneous flow experiments in a quasi-two-dimensional porous medium and found $a \approx 0.5$ in Equation 4. Rassi et al. (2011) measured an exponent a between 0.3 and 0.45 depending on the fluid saturation from steady-state two-phase flow in bead packs. Sinha et al. (2017) also conducted experiments and simulations and proposed a power-law flow regime with an exponent $a = 0.5$.

High-resolution X-ray tomography has allowed the fluid configurations to be imaged inside porous materials to interpret the physical origin of this nonlinear regime, which is due to the intermittent occupancy of regions of the pore space by the two phases that facilitates flow (Gao et al., 2017, 2020; Spurin et al., 2019a, 2019b).

From a theoretical perspective, Sinha and Hansen (2012) suggested that the exponent a was around 0.5 and confirmed this behavior using a dynamic pore-scale model. Roy et al. (2019) proposed a size dependence of the non-linear regime, such that for larger systems, the transition from intermittency to linear flow occurred for lower Ca in a high flow rate regime. In the limit of an infinite system, this suggests that there is no linear Darcy regime at all. Gao et al. (2020) quantified the threshold capillary number for the onset of intermittency Ca^i as $\sim 10^{-5}$ and found $a = 0.6$ from experiments of steady-state flow on water-wet Bentheimer sandstone for $f_w = 0.5$; however, there were only eight data points. Overall, despite this body of theoretical, numerical, and experimental work, there is no accurate quantification of when the transition to nonlinear flow occurs and the relationship between pressure gradient and flow rate in this intermittent regime.

In this paper, we study steady-state immiscible two-phase flow through a water-wet Bentheimer sandstone sample with different flow rates (capillary number varies from $\sim 10^{-7}$ to $\sim 10^{-4}$) and fractional flows during an imbibition displacement ($f_w = 0.2$, 0.4, 0.5, 0.6, 0.8, and 1). We quantify the threshold capillary number for the onset of the power-law non-Darcy regime, Equation 4, and measure the exponent a, which we find to be a function of fractional flow. We use energy balance to predict accurately the onset of non-Darcy flow as a function of capillary number and fractional flow, and for different rocks and viscosity ratios.

2. Materials and Methods

We performed experiments on a water-wet Bentheimer sandstone sample (5.97-mm diameter and 27.88-mm length) mounted in a specially designed core flooding system: details of the experimental apparatus can be found in the literature (Gao et al., 2017, 2020). A long sample was chosen to allow an accurate measurement of pressure drop. The diameter was chosen to be consistent with previous work (Gao et al., 2020) where pressure measurements were combined with pore-scale imaging. Further details about Bentheimer sandstone and associated pore-scale images can be found in Muljadi (2015). The wetting phase was 15 wt % KI (potassium iodide) brine, and the nonwetting phase was *n*-decane, both injected by high-precision ISCO

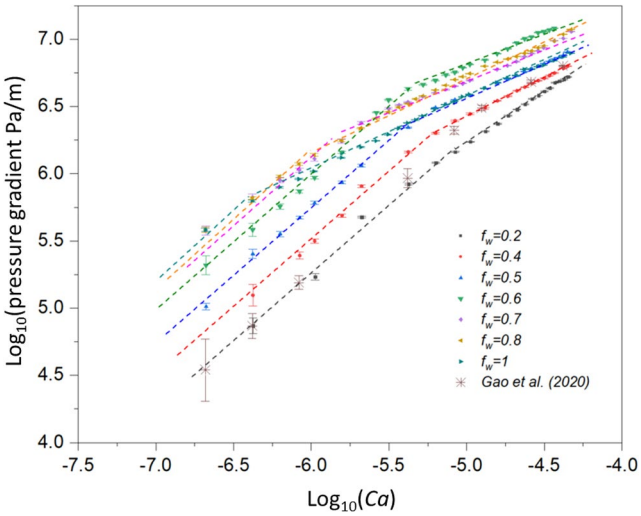

Figure 1. The measured pressure gradients ∇P as a function of capillary number Ca, Equation 3, for different fractional flows, f_w: 0.2, 0.4, 0.5, 0.6, 0.7, 0.8, and 1; also shown are the experimental results of Gao et al. (2020), where $f_w = 0.5$. The error bars reflect the standard deviation in the measurement of pressure gradient.

pumps. To ensure uniform flow at the inlet, we used a dual injection port (Gao et al., 2019); this provides a more even flow than T-junction injection used in previous studies which may have over-stated the degree of intermittent flow as a consequence (Gao et al., 2020).

During the flow, the pressure gradient between inlet and outlet of the sample was measured by a high-precision pressure transducer Keller PD-33X. The viscosity of the brine $\mu_w = 0.821$ mPa s, the n-decane viscosity $\mu_{nw} = 0.838$ mPa s (PubChem, open chemistry database), while the interfacial tension was measured to be $\sigma = 47$ mN/m. The absolute permeability for the sample was $K = 1.85(\pm 0.02) \times 10^{-12}$ m^2, measured from the relationship between flow rate and pressure gradient when the core was fully saturated with brine. We then injected n-decane at 3 ml/min for 30 min to reach the initial brine saturation.

We started the two-phase flow experiment by injecting the two phases at a fractional flow f_w of 0.2 at 0.04 ml/min total flow rate ($Ca = 4.2 \times 10^{-7}$); the pressure gradient was recorded after 10 h when it stabilized, and then we gradually increased the flow rate from low to high and recorded the pressure gradients at steady state. A stable pressure difference was used to determine that the system was at steady state. The time for the pressure gradient to become constant depended on the flow rates: it was up to 10 h for the low flow rates (<0.04 ml/min) but as little as 5 min for high flow rate flooding (greater than 3 ml/min). The highest flow rate was 4.25 ml/min ($Ca = 4.5 \times 10^{-5}$).

Once we had reached the highest flow rate for a given fractional flow, we injected n-decane at 3 ml/min for 30 min again to return to the initial saturation. We repeated the injection sequence at a series of increasing flow rates for other fractional flows: 0.4, 0.5, 0.6, 0.7, 0.8, and 1; we studied seven fractional flows with 20–30 measurements at different rates for each fractional flow, making a total of 178 measurements.

3. Results and Discussion

3.1. The Nonlinear Flow Regime

The results, Figure 1, show that Ca is proportional to the pressure gradient ∇P at low flow rates: $\nabla P \sim Ca$ with $a = 1$ is valid for all the fractional flows studied for sufficiently small Ca. However, in all cases, this is followed by a nonlinear regime, Equation 4. The exponent a is a function of the fractional flow, see Table 1: the highest value $a = 0.74 \pm 0.02$ occurs when $f_w = 0.2$, which displayed the lowest degree of intermittency defined as the deviation from a linear Darcy law; $f_w = 0.6$ had the lowest exponent $a = 0.44 \pm 0.02$ indicating a strong deviation from linear flow.

Table 1
Summary of the Exponent a for $\nabla P \sim Ca^a$, Threshold Capillary Number Ca^i, the Associated Nonwetting Phase Capillary Number Ca^i_{nw}, and the Wetting Phase Capillary Number Ca^i_w for the Onset of Intermittency, See Figure 1

Fractional flow (f_w)	Exponent a ($Ca < Ca^i$)	Ca^i	Ca^i_{nw}	Ca^i_w	Exponent a ($Ca > Ca^i$)
0.2	1	$\sim 10^{-5.1}$	$\sim 10^{-5.2}$	$\sim 10^{-5.8}$	0.74 ± 0.02
0.4	1	$\sim 10^{-5.2}$	$\sim 10^{-5.4}$	$\sim 10^{-5.6}$	0.57 ± 0.02
0.5	1	$\sim 10^{-5.3}$	$\sim 10^{-5.5}$	$\sim 10^{-5.5}$	0.48 ± 0.02
0.6	1	$\sim 10^{-5.4}$	$\sim 10^{-5.8}$	$\sim 10^{-5.6}$	0.44 ± 0.02
0.7	1	$\sim 10^{-5.5}$	$\sim 10^{-6.0}$	$\sim 10^{-5.7}$	0.47 ± 0.02
0.8	1	$\sim 10^{-5.7}$	$\sim 10^{-6.3}$	$\sim 10^{-5.8}$	0.56 ± 0.02
1	1	$\sim 10^{-6.4}$	—	$\sim 10^{-6.4}$	0.66 ± 0.02

These observations are consistent with previous experiments where the rock and fluids were imaged at micron resolution, which concluded that intermittency, or a fluctuating pore occupancy, only constituted a small percentage of the total pore volume for $f_w < 0.5$ (Spurin et al., 2019a). Moreover, in our experiments, when $f_w < 0.5$, the pressure gradient increased with fractional flow indicating that the total mobility decreases; for $f_w > 0.5$, a more complex behavior emerged, where curves of ∇P as a function of Ca for constant f_w crossed each other, indicating a significant increase in mobility with flow rate for the intermediate fractional flows, were both phases compete to occupy high-conductivity paths through the pore space (Gao et al., 2020).

The threshold capillary number Ca^i between the linear Darcy regime and intermittent flow, Table 1, is also a function of the fractional flow: Ca^i

decreased from $\sim 10^{-5.1}$ to $\sim 10^{-6.4}$ as the fractional flow f_w increased from 0.2 to 1. Thus, higher fractional flows have a lower critical flow rate q_t^i for the onset of intermittency. Note that the results for a fractional flow of 1 represent the capillary desaturation process (Lake, 1989); at steady state, there is only one mobile phase.

3.2. Quantification of the Transition From Linear to Intermittent Flow

We assume that we see the onset of intermittency when the energy, associated with the injection of fluids over a characteristic length l, related to the distance between pores, is first matched by the change in surface energy needed to create a fluid meniscus (Blunt, 2017; Cueto-Felgueroso & Juanes, 2016; Gao et al., 2020). The interfacial energy required to form an interface between the fluids inside a single pore is of order σr^2 where r is a typical pore radius. The mechanical (PdV) work occurs over a volume l^3 or a pore volume of $dV = \phi l^3$ where ϕ is the porosity. The change in pressure, P, across this length is $-l\nabla P$ where ∇P is the pressure gradient. The mechanical work PdV is therefore $-\phi l^4 \nabla P$. Hence, intermittency first occurs when the interfacial and mechanical energies match, or

$$\sigma r^2 \sim -\phi l^4 \nabla P. \tag{5}$$

We now need to estimate ∇P over a typical pore length. We can assume a Darcy-like flow, although we need to note that we apply it at the pore scale. In imaging experiments, intermittency is caused by the nonwetting phase periodically finding more conductive pathways through the pore space (Gao et al., 2020; Spurin et al., 2019b). We assume that since both phases have to move, the pressure gradient necessary to allow intermittency is controlled by the total threshold flow rate q_t^i. The limiting mobility is assumed to be $(1 - f_w)/\mu_w$, governed by the flow of the wetting phase into and out of pores filled with nonwetting phase with an effective relative permeability, at least in the viscous-flow limit, of $1 - f_w$, or the nonwetting phase fractional flow. Hence, from Equation 1, we estimate $\nabla P \approx -\mu_w q_t^i / K(1 - f_w)$. We then expect the onset of intermittency from Equation 5, when

$$\sigma r^2 = \frac{\mu_w q_t^i \phi l^4}{K(1 - f_w)}. \tag{6}$$

This can be rearranged to write the threshold capillary numbers $Ca_w^i = \mu_w f_w q_t^i / \sigma$ and $Ca_{nw}^i = \mu_{nw}(1 - f_w) q_t^i / \sigma$ as follows:

$$Ca_{nw}^i = Y^i (1 - f_w)^2 \tag{7}$$

and

$$Ca_w^i = Y^i f_w (1 - f_w) \frac{\mu_w}{\mu_{nw}}, \tag{8}$$

where the dimensionless number Y^i is defined by

$$Y^i = \frac{\mu_{nw}}{\mu_w} \frac{Kr^2}{\phi l^4}. \tag{9}$$

Note that Y^i incorporates information on both pore structure and viscosity ratio. In our experiments, for Bentheimer sandstone, the porosity ϕ is 0.2, the mean pore radius r is 24 μm (Blunt, 2017), while to capture the onset of intermittency l has a value of ~150 μm (Gao et al., 2020): l is the mean pore-to-pore distance obtained from a pore-network analysis of the pore structure (Raeini et al., 2017). Then using the fluid viscosities in this experiment we calculate $Y^i \approx 10^{-5}$.

In Figure 2, we delineate the threshold between Darcy-like and intermittent flow using Equations 7 and 8 which provides an accurate prediction compared to the values in Table 1. Note, however, that Equations 7 and 8 are only valid when we strictly have multiphase flow with $1 > f_w > 0$ and cannot be applied for $f_w = 1$ or 0.

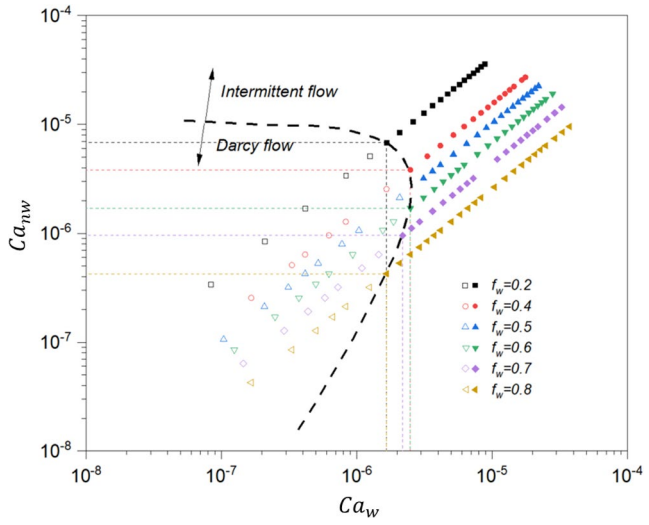

Figure 2. The phase diagram of the transition from Darcy flow (empty symbols) to intermittent flow (filled symbols) as a function of nonwetting phase capillary number Ca^i_{nw} and wetting phase capillary number Ca^i_w; the dashed line is the predicted threshold using Equations 7 and 8.

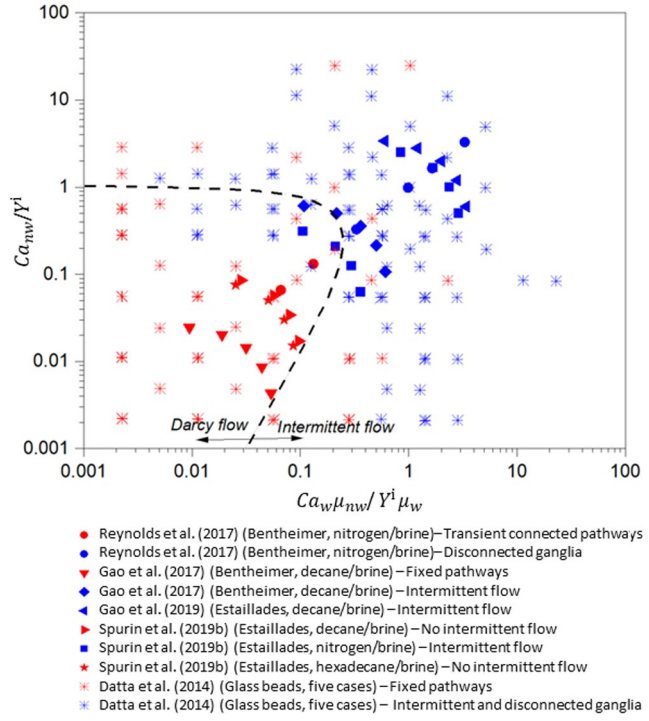

Figure 3. The replotted phase diagram of the transition from connected pathway flow (Darcy flow, Equations 1 and 2) to no connected pathways (intermittent flow, Equation 4) using literature data (Datta et al., 2014a; Gao et al, 2017, 2019; Reynolds et al., 2017; Spurin et al., 2019b) where different viscosity fluids were injected into different rocks; full details can be found in Table 2. In these experiments, the pressure gradient was not measured; instead the onset of intermittent flow was estimated from the pore-scale dynamics as described in the legend. The dashed line is the predicted threshold from Equations 7 and 8.

Our experiments were performed for one set of fluids with almost equal viscosities. To test the applicability of our theoretical result for different fluids, we apply Equation 9 to the data from Reynolds et al. (2017). As in this work, the rock studied was Bentheimer sandstone, so that the geometric terms in Equation 9 are the same. We show again that we make accurate predictions where we calculate $Y^i = 10^{-6.5}$, for nitrogen and brine injection: the threshold line (Figure 3) between Darcy and intermittent flow is consistent with the X-ray pore-scale images described in Reynolds et al. (2017).

Furthermore, we also apply our theory to a different rock sample, Estaillades carbonate with both low (nitrogen and brine, $\mu_{nw}/\mu_w = 0.026$) and high (hexadecane and brine, $\mu_{nw}/\mu_w = 4.21$) viscosity ratio fluids; here $\phi = 0.295$, $r = 7.5$ μm, $K = 1.49 \times 10^{-13}$ m^2, and l has a value of ~63 μm (here the pore length is assumed to be the inverse of the cube root of the number of pores per unit volume, while the radius is found from a pore-network analysis) (Blunt, 2017): Equation 9 is used to calculate $Y^i = 10^{-7.3}$ and $10^{-5.1}$, respectively. The predicted thresholds are consistent with the results of Spurin et al. (2019b) where X-ray scanning results showed that the low viscosity ratio fluid system displayed strong intermittency, but no intermittency was observed at the pore scale for the high fluid viscosity ratio case although the total capillary numbers were similar. Estaillades has a more heterogeneous pore space with a wider range of pore size than Bentheimer sandstone (Blunt, 2017), and yet we still accurately capture the onset of intermittency for this rock.

We finally apply our theory to other data in the literature for Bentheimer sandstone, Estaillades limestone and glass bead packs (Datta et al., 2014a;Gao et al., 2017, 2019): details are provided in Figure 3 and Table 2. For a bead pack, we estimate $l = D\phi/(1-\phi)$ (Blunt, 2017; Porta et al., 2015; Whitaker, 2013), where D is the bead diameter; the radius, r, is assumed to be $l/2$. The permeability K can be estimated from the Kozeny-Carman equation $K = \phi^3 D^2/180(1-\phi)^2$ (Blunt, 2017). In all cases, we predict the onset of intermittency, as demonstrated in Figure 3, with only a few discrepancies for the bead pack data. Note, however, that in the experiments pressure gradient was not measured, and so the onset of intermittency was determined from an analysis of the pore-scale dynamics as described in the legend of the figure.

4. Conclusions

We have measured the pressure gradient as a function of flow rate for different fractional flows of oil and brine through a small sample of Bentheimer sandstone. We have observed the Darcy flow regime and the transition to non-Darcy or intermittent flow. At low flow rates, the flow follows a standard linear Darcy law, while for higher flow rates we see $\nabla P \sim Ca^a$. We proposed a relationship for the threshold capillary number for the onset of intermittent flow, Equations 7 and 8, which accurately matched the experimental results and is applicable to the different viscosity ratio fluids and different rock types, reconciling a large body of experimental results in the literature.

Future work could include the study of flow at different viscosity ratios, system lengths, mixed-wet and oil-wet media, and different types of porous material. We could also study what controls intermittency and the

Table 2
Summary of the Pore Geometry Properties, Fluid Viscosities, and Calculated Values of Y^i, Equation 9, for Different Porous Media: The Predicted Onset of Intermittency is Compared to the Experimental Results in Figure 3

Porous medium	ϕ	r (μm)	K (10^{-12} m^2)	l (μm)	μ_{nw} (mPa s)	μ_w (mPa s)	Y^i
Bentheimer[a]	0.20	24	1.85	150	0.021	0.642	$10^{-6.5}$
Bentheimer[b]	0.20	24	1.85	150	0.838	0.821	$10^{-5.0}$
Estaillades[c,d]	0.295	7.5	0.15	63	0.838	0.821	$10^{-5.7}$
Estaillades[d]	0.295	7.5	0.15	63	0.021	0.821	$10^{-7.3}$
Estaillades[d]	0.295	7.5	0.15	63	3.45	0.821	$10^{-5.1}$
Glass beads[e]	0.41	12.5	1.43	25	16.8	110	$10^{-3.7}$
Glass beads[e]	0.41	12.5	1.43	25	16.8	2.70	$10^{-2.1}$
Glass beads[e]	0.41	21	3.96	41	16.8	2.70	$10^{-2.1}$

[a]Reynolds et al. (2017). [b]Gao et al. (2017). [c]Gao et al. (2019). [d]Spurin et al. (2019b). [e]Dattaet al.(2014a).

power-law exponent in Equation 4, including the balance of viscous, inertial and capillary forces (Ferrari & Lunati, 2013), and shear-stress at the fluid-fluid interface (Roman et al., 2020; Zarikos et al., 2018).

Data Availability Statement

The experimental data are available from https://data.mendeley.com/datasets/kgsh9nsdr4.

Acknowledgment
The authors gratefully acknowledge funding from the Shell Digital Rocks program at Imperial College London.

References

Armstrong, R. T., & Berg, S. (2013). Interfacial velocities and capillary pressure gradients during Haines jumps. *Physical Review E*, *88*(4), 043010.
Berg, S., Ott, H., Klapp, S. A., Schwing, A., Neiteler, R., Brussee, N., et al. (2013). Real-time 3d imaging of Haines jumps in porous media flow. *Proceedings of the National Academy of Sciences of the United States of America*, *110*(10), 3755–3759.
Blunt, M. J. (2017). *Multiphase flow in permeable media: A pore-scale perspective.*. Cambridge, UK: Cambridge University Press.
Cueto-Felgueroso, L., & Juanes, R. (2016). A discrete-domain description of multiphase flow in porous media: Rugged energy landscapes and the origin of hysteresis. *Geophysical Research Letters*, *43*, 1615–1622. https://doi.org/10.1002/2015GL067015
Datta, S. S., Dupin, J.-B., & Weitz, D. A. (2014a). Fluid breakup during simultaneous two-phase flow through a three-dimensional porous medium. *Physics of Fluids*, *26*(6), 062004.
Datta, S. S., Ramakrishnan, T., & Weitz, D. A. (2014b). Mobilization of a trapped non-wetting fluid from a three-dimensional porous medium. *Physics of Fluids*, *26*(2), 022002.
Ferrari, A., & Lunati, I. (2013). Direct numerical simulations of interface dynamics to link capillary pressure and total surface energy. *Advances in Water Resources*, *57*, 19–31.
Gao, Y., Lin, Q., Bijeljic, B., & Blunt, M. J. (2017). X-ray microtomography of intermittency in multiphase flow at steady state using a differential imaging method. *Water Resources Research*, *53*, 10274–10292. https://doi.org/10.1002/2017WR021736
Gao, Y., Lin, Q., Bijeljic, B., & Blunt, M. J. (2020). Pore-scale dynamics and the multiphase Darcy law. *Physical Review Fluids*, *5*(1), 013801.
Gao, Y., Raeini, A. Q., Blunt, M. J., & Bijeljic, B. (2019). Pore occupancy, relative permeability and flow intermittency measurements using x-ray micro-tomography in a complex carbonate. *Advances in Water Resources*, *129*, 56–69.
Gjennestad, M. A., Winkler, M., & Hansen, A. (2020). Pore network modeling of the effects of viscosity ratio and pressure gradient on steady-state incompressible two-phase flow in porous media. *Transport in Porous Media*, *132*, 355–379
Iglauer, S., Paluszny, A., Rahman, T., Zhang, Y., Wülling, W., & Lebedev, M. (2019). Residual trapping of CO_2 in an oil-filled, oil-wet sandstone core: Results of three-phase pore-scale imaging. *Geophysical Research Letters*, *46*, 11146–11154. https://doi.org/10.1029/2019GL083401
Lake, L. W. (1989). *Enhanced oil recovery. Old Tappan*. NJ: Prentice Hall Inc.
Muljadi, B. P. (2015). *Bentheimer sandstone*. Retrieved From http://www.digitalrocksportal.org/projects/11. https://doi.org/10.17612/P77P49
Muskat, M. (1937). *The flow of homogeneous fluids through porous media*. New York, NY: McGraw-Hill Book.
Muskat, M., & Meres, M. W. (1936). The flow of heterogeneous fluids through porous media. *Physics*, *7*(9), 346–363.
Pak, T., Butler, I. B., Geiger, S., van Dijke, M. I., & Sorbie, K. S. (2015). Droplet fragmentation: 3d imaging of a previously unidentified pore-scale process during multiphase flow in porous media. *Proceedings of the National Academy of Sciences of the United States of America*, *112*(7), 1947–1952.
Porta, G. M., Bijeljic, B., Blunt, M., & Guadagnini, A. (2015). Continuum-scale characterization of solute transport based on pore-scale velocity distributions. *Geophysical Research Letters*, *42*, 7537–7545. https://doi.org/10.1002/2015GL065423
Raeini, A. Q., Bijeljic, B., & Blunt, M. J. (2017). Generalized network modeling: Network extraction as a coarse-scale discretization of the void space of porous media. *Physical Review E*, *96*(1), 013312.
Rassi, E. M., Codd, S. L., & Seymour, J. D. (2011). Nuclear magnetic resonance characterization of the stationary dynamics of partially saturated media during steady-state infiltration flow. *New Journal of Physics*, *13*(1), 015007.
Reynolds, C., & Krevor, S. (2015). Characterizing flow behavior for gas injection: Relative permeability of CO_2-brine and N_2-water in heterogeneous rocks. *Water Resources Research*, *51*, 9464–9489. https://doi.org/10.1002/2015WR018046

Reynolds, C., Menke, H., Andrew, M., Blunt, M. J., & Krevor, S. (2017). Dynamic fluid connectivity during steady-state multiphase flow in a sandstone. *Proceedings of the National Academy of Sciences of the United States of America*, *114*(31), 8187–8192.

Roman, S., Soulaine, C., & Kovscek, A. R. (2020). Pore-scale visualization and characterization of viscous dissipation in porous media. *Journal of Colloid and Interface Science*, *558*, 269–279.

Roy, S., Sinha, S., & Hansen, A. (2019). Immiscible two-phase flow in porous media: Effective rheology in the continuum limit. arXiv:1912.05248.

Rücker, M., Berg, S., Armstrong, R., Georgiadis, A., Ott, H., Schwing, A., et al. (2015). From connected pathway flow to ganglion dynamics. *Geophysical Research Letters*, *42*, 3888–3894. https://doi.org/10.1002/2015GL064007

Sinha, S., Bender, A. T., Danczyk, M., Keepseagle, K., Prather, C. A., Bray, J. M., et al. (2017). Effective rheology of two-phase flow in three-dimensional porous media: Experiment and simulation. *Transport in Porous Media*, *119*(1), 77–94.

Sinha, S., & Hansen, A. (2012). Effective rheology of immiscible two-phase flow in porous media. *EPL (Europhysics Letters)*, *99*(4), 44004.

Spurin, C., Bultreys, T., Bijeljic, B., Blunt, M. J., & Krevor, S. (2019a). Intermittent fluid connectivity during two-phase flow in a heterogeneous carbonate rock. *Physical Review E*, *100*(4), 043103.

Spurin, C., Bultreys, T., Bijeljic, B., Blunt, M. J., & Krevor, S. (2019b). Mechanisms controlling fluid breakup and reconnection during two-phase flow in porous media. *Physical Review E*, *100*(4), 043115.

Tallakstad, K. T., Knudsen, H. A., Ramstad, T., Løvoll, G., Måløy, K. J., Toussaint, R., & Flekkøy, E. G. (2009). Steady-state two-phase flow in porous media: Statistics and transport properties. *Physical Review Letters*, *102*(7), 074502.

Whitaker, S. (2013). The method of volume averaging (Vol. 13). Berlin, Germany: Springer Science & Business Media.

Zarikos, I., Terzis, A., Hassanizadeh, S., & Weigand, B. (2018). Velocity distributions in trapped and mobilized non-wetting phase ganglia in porous media. *Scientific Reports*, *8*(1), 13228.

Zhang, Y., Lebedev, M., Jing, Y., Yu, H., & Iglauer, S. (2019). In-situ x-ray micro-computed tomography imaging of the microstructural changes in water-bearing medium rank coal by supercritical co2 flooding. *International Journal of Coal Geology*, *203*, 28–35.

Zhao, B., Pahlavan, A. A., Cueto-Felgueroso, L., & Juanes, R. (2018). Forced wetting transition and bubble pinch-off in a capillary tube. *Physical Review Letters*, *120*(8), 084501.